ATLAS PUB Note
ATL-PHYS-PUB-2022-036
4th July 2022

Dark matter summary plots for *s*-channel, 2HDM+*a* and Dark Higgs models

The ATLAS Collaboration

This is an update of summary plots from the Exotics, SUSY, HDBS and Higgs working groups, via the CDM sub-group, for dark matter simplified models with *s*-channel Spin-1 and Spin-0 mediators, a Two-Higgs-Doublet model with an extra pseudoscalar mediator (2HDM+*a*) and a Dark Higgs model. Results shown are current as of July 2022.

1 Introduction

This document provides updated summary plots of mediator-based dark matter models, including s-channel models [1], a 2HDM+a model [2] and a Dark Higgs model [3] using results current as of July 2022. Results for s-channel models are discussed in Section 2. The 2HDM+a model is discussed in Section 3. The Dark Higgs model is discussed in Section 4.

2 s-channel summary plots

Spin-1 mediators are discussed in Section 2.1 and spin-0 mediators are discussed in Section 2.2.

2.1 Spin-1 Mediators

With respect to the summary results for spin-1 mediators released in December 2021 for the Moriond 2022 conferences [4], no major modifications have been made. The search for dark matter in association with a leptonically decaying Z boson, denoted $E_{\mathrm{T}}^{\mathrm{miss}} + Z(\ell^+\ell^-)$ has been published in [5] so the corresponding reference in each plot has been updated. This modification appears in Figure 1, Figure 2, Figure 5, Figure 6, Figure 9, Figure 10 and Figure 13.

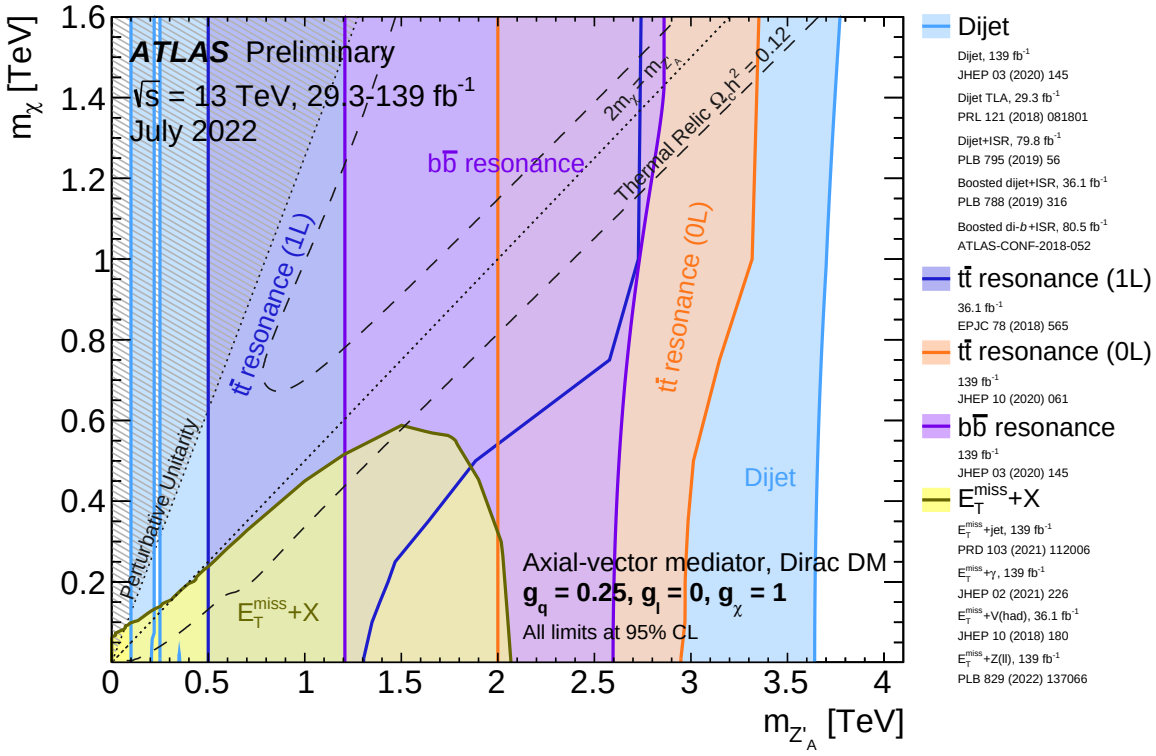

Figure 1: Regions in the (mediator-mass, DM-mass) plane excluded at 95% CL by visible and invisible searches, for leptophobic axial-vector mediator simplified models. Each shaded region represents the union of the exclusion contours of the individual analyses listed in the legend, where more than one result contributes. The exclusions are computed for a DM coupling $g_\chi = 1$, quark coupling $g_q = 0.25$, universal to all flavours, and no coupling to leptons. Dashed curves labelled "thermal relic" correspond to combinations of DM and mediator mass values that are consistent with a DM density of $\Omega h^2 = 0.12$ and a standard thermal history, as computed in MadDM [Phys. Dark Univ. **26** (2019) 100377, AIP Conf. Proc. **1743** (2016) 1, 060001]. Between the two curves, annihilation processes described by the simplified model deplete Ωh^2 to below 0.12. A dotted line indicates the kinematic threshold where the mediator can decay on-shell into DM. Excluded regions that are in tension with the perturbative unitary considerations of [JHEP **02** (2016) 016] are indicated by shading in the upper left corner. The reinterpretation procedure for the TLA analysis follows the procedure recommended by ATLAS in Appendix A of [Phys. Rev. D **91** (2015) 052007], while the high-mass dijet and dijet+ISR analyses are reinterpreted following [Phys. Lett. B **769** (2017) 520].

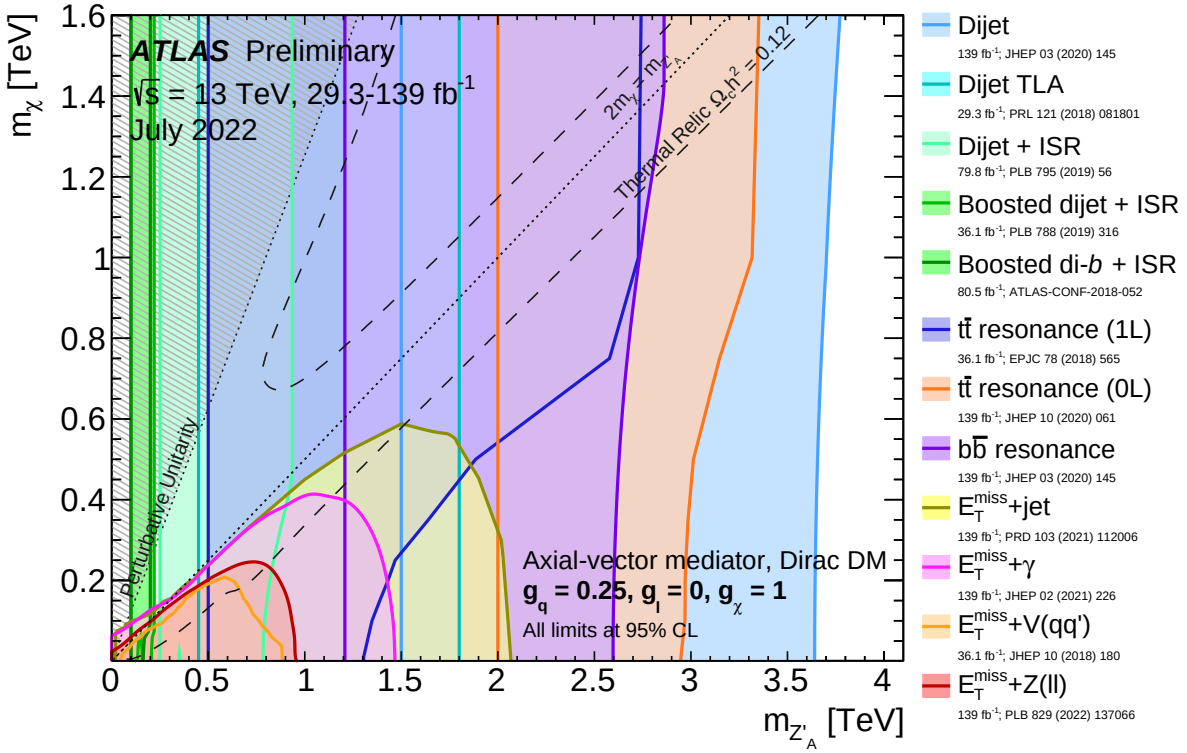

Figure 2: Regions in the (mediator-mass, DM-mass) plane excluded at 95% CL by visible and invisible searches, for leptophobic axial-vector mediator simplified models. The exclusions are computed for a DM coupling $g_\chi = 1$, quark coupling $g_q = 0.25$, universal to all flavours, and no coupling to leptons. Dashed curves labelled "thermal relic" correspond to combinations of DM and mediator mass values that are consistent with a DM density of $\Omega h^2 = 0.12$ and a standard thermal history, as computed in MadDM [Phys. Dark Univ. **26** (2019) 100377, AIP Conf. Proc. **1743** (2016) 1, 060001]. Between the two curves, annihilation processes described by the simplified model deplete Ωh^2 to below 0.12. A dotted line indicates the kinematic threshold where the mediator can decay on-shell into DM. Excluded regions that are in tension with the perturbative unitary considerations of [JHEP **02** (2016) 016] are indicated by shading in the upper left corner. The reinterpretation procedure for the TLA analysis follows the procedure recommended by ATLAS in Appendix A of [Phys. Rev. D **91** (2015) 052007], while the high-mass dijet and dijet+ISR analyses are reinterpreted following [Phys. Lett. B **769** (2017) 520].

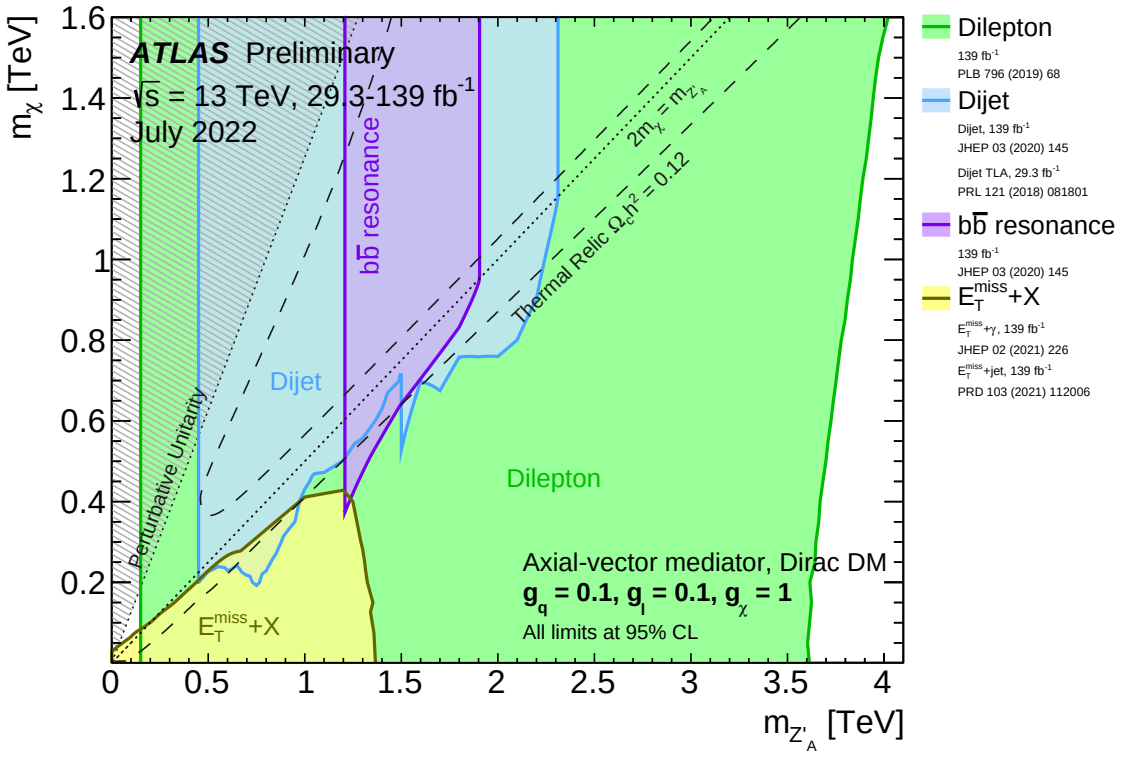

Figure 3: Regions in the (mediator-mass, DM-mass) plane excluded at 95% CL by visible and invisible searches, for leptophilic axial-vector mediator simplified models. Each shaded region represents the union of the exclusion contours of the individual analyses listed in the legend, where more than one result contributes. The exclusions are computed for a DM coupling $g_\chi = 1$, quark coupling $g_q = 0.1$, and lepton coupling $g_l = 0.1$, in both cases universal to all flavours. Dashed curves labelled "thermal relic" correspond to combinations of DM and mediator mass values that are consistent with a DM density of $\Omega h^2 = 0.12$ and a standard thermal history, as computed in MadDM [Phys. Dark Univ. **26** (2019) 100377, AIP Conf. Proc. **1743** (2016) 1, 060001]. Between the two curves, annihilation processes described by the simplified model deplete Ωh^2 to below 0.12. A dotted line indicates the kinematic threshold where the mediator can decay on-shell into DM. Excluded regions that are in tension with the perturbative unitary considerations of [JHEP **02** (2016) 016] are indicated by shading in the upper left corner.

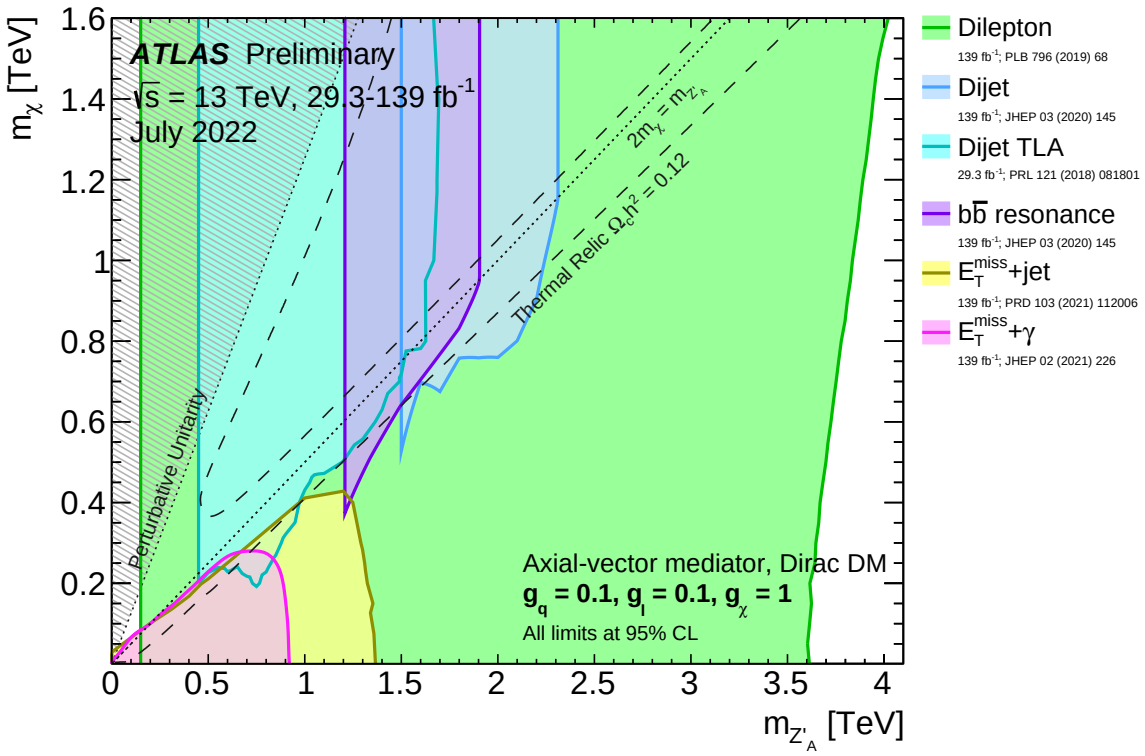

Figure 4: Regions in the (mediator-mass, DM-mass) plane excluded at 95% CL by visible and invisible searches, for leptophilic axial-vector mediator simplified models. The exclusions are computed for a DM coupling $g_\chi = 1$, quark coupling $g_q = 0.1$, and lepton coupling $g_l = 0.1$, in both cases universal to all flavours. Dashed curves labelled "thermal relic" correspond to combinations of DM and mediator mass values that are consistent with a DM density of $\Omega h^2 = 0.12$ and a standard thermal history, as computed in MadDM [Phys. Dark Univ. **26** (2019) 100377, AIP Conf. Proc. **1743** (2016) 1, 060001]. Between the two curves, annihilation processes described by the simplified model deplete Ωh^2 to below 0.12. A dotted line indicates the kinematic threshold where the mediator can decay on-shell into DM. Excluded regions that are in tension with the perturbative unitary considerations of [JHEP **02** (2016) 016] are indicated by shading in the upper left corner.

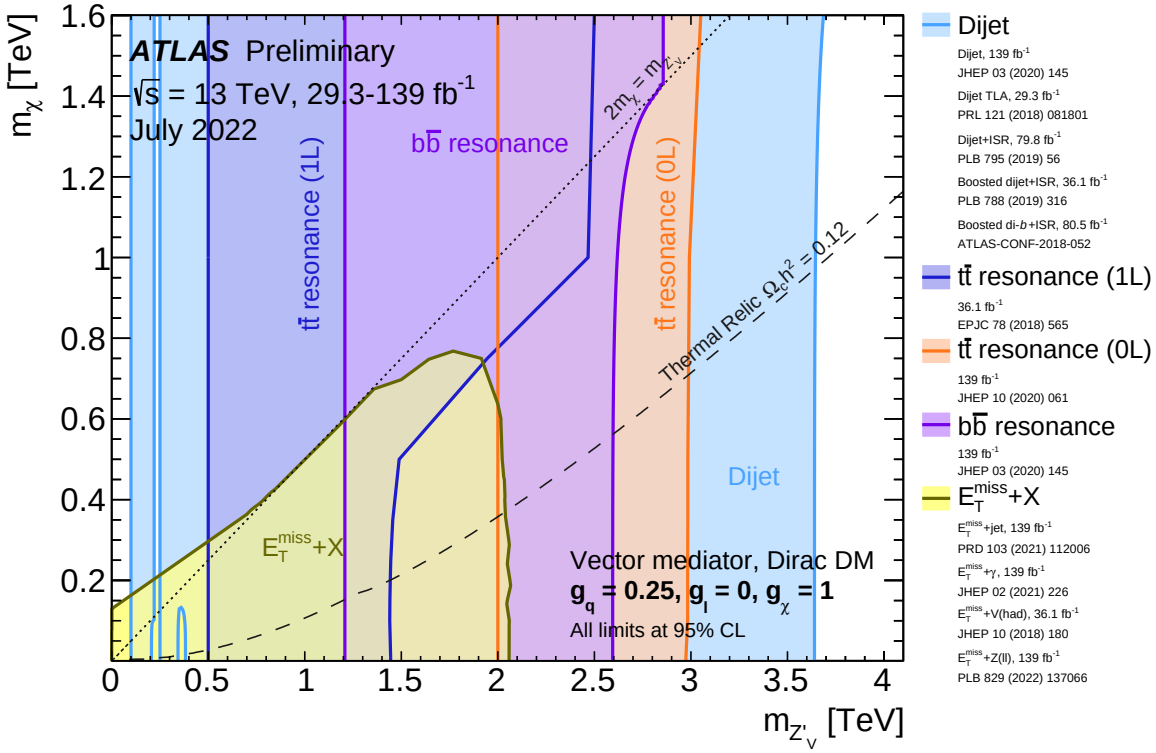

Figure 5: Regions in the (mediator-mass, DM-mass) plane excluded at 95% CL by dijet, dilepton and $E_{\mathrm{T}}^{\mathrm{miss}}$+$X$ searches, for leptophobic vector mediator simplified models. Each shaded region represents the union of the exclusion contours of the individual analyses listed in the legend, where more than one result contributes. The exclusions are computed for a DM coupling $g_\chi = 1$, quark coupling $g_q = 0.25$, universal to all flavours, and no coupling to leptons. Dashed curves labelled "thermal relic" correspond to combinations of DM and mediator mass values that are consistent with a DM density of $\Omega h^2 = 0.12$ and a standard thermal history as computed in MadDM [Phys. Dark Univ. **26** (2019) 100377, AIP Conf. Proc. **1743** (2016) 1, 060001]. Above the curve, annihilation processes described by the simplified model deplete Ωh^2 to below 0.12. The dotted line indicates the kinematic threshold where the mediator can decay on-shell into DM. The reinterpretation procedure for the TLA analysis follows the procedure recommended by ATLAS in Appendix A of [Phys. Rev. D **91** (2015) 052007], while the high-mass dijet and dijet+ISR analyses are reinterpreted following [Phys. Lett. B **769** (2017) 520].

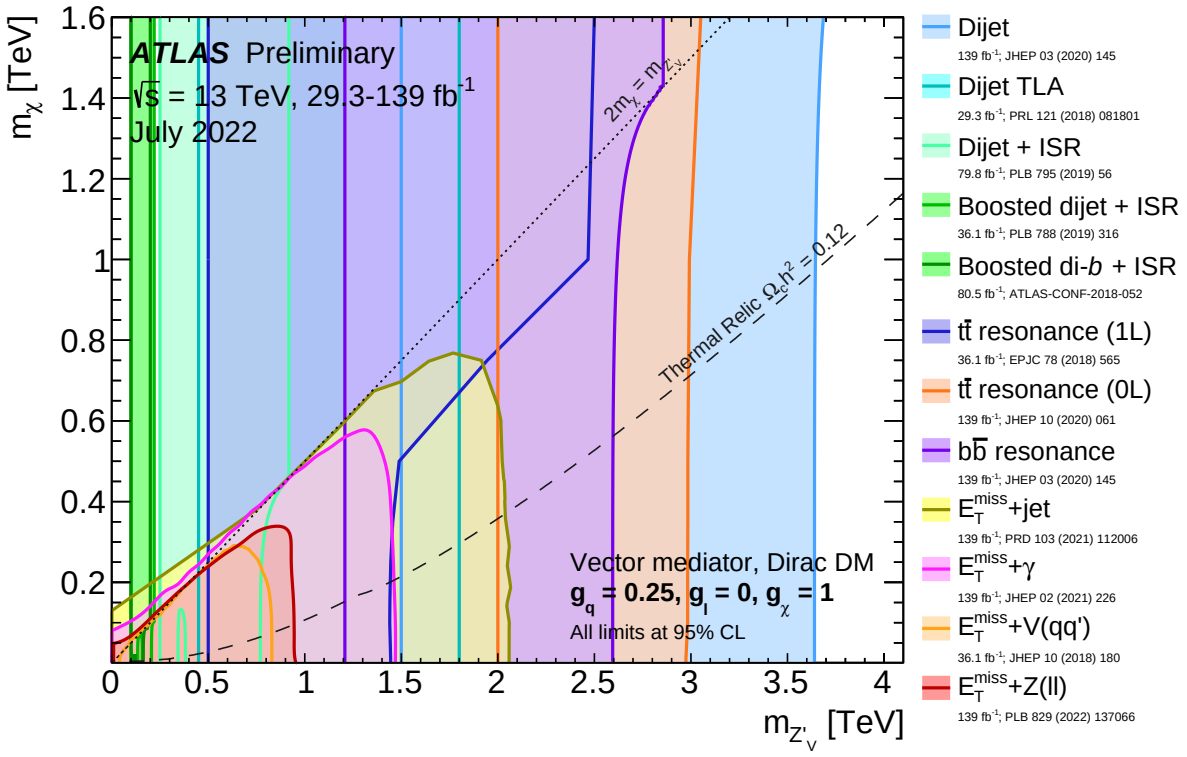

Figure 6: Regions in the (mediator-mass, DM-mass) plane excluded at 95% CL by dijet, dilepton and $E_{\mathrm{T}}^{\mathrm{miss}}$+$X$ searches, for leptophobic vector mediator simplified models. The exclusions are computed for a DM coupling $g_{\chi} = 1$, quark coupling $g_q = 0.25$, universal to all flavours, and no coupling to leptons. Dashed curves labelled "thermal relic" correspond to combinations of DM and mediator mass values that are consistent with a DM density of $\Omega h^2 = 0.12$ and a standard thermal history as computed in MadDM [Phys. Dark Univ. **26** (2019) 100377, AIP Conf. Proc. **1743** (2016) 1, 060001]. Above the curve, annihilation processes described by the simplified model deplete Ωh^2 to below 0.12. The dotted line indicates the kinematic threshold where the mediator can decay on-shell into DM. The reinterpretation procedure for the TLA analysis follows the procedure recommended by ATLAS in Appendix A of [Phys. Rev. D **91** (2015) 052007], while the high-mass dijet and dijet+ISR analyses are reinterpreted following [Phys. Lett. B **769** (2017) 520].

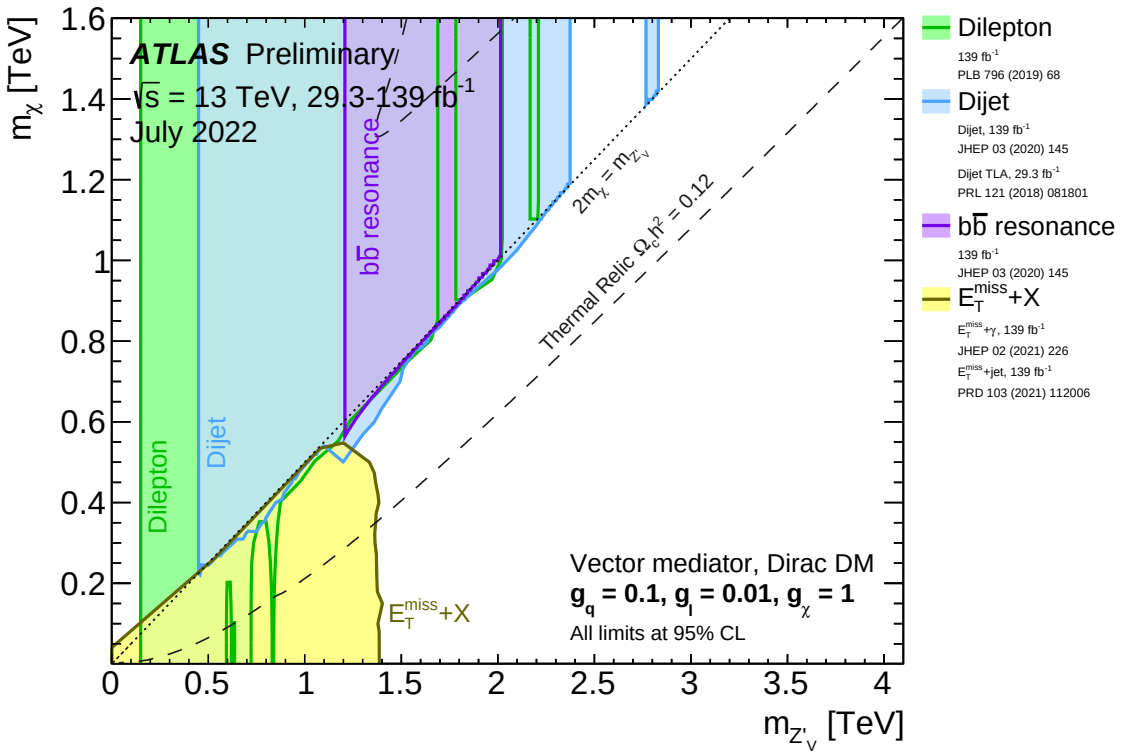

Figure 7: Regions in the (mediator-mass, DM-mass) plane excluded at 95% CL by dijet, dilepton and $E_{\mathrm{T}}^{\mathrm{miss}}+X$ searches, for leptophilic vector mediator simplified models. Each shaded region represents the union of the exclusion contours of the individual analyses listed in the legend, where more than one result contributes. The exclusions are computed for a DM coupling $g_{\chi} = 1$, quark coupling $g_q = 0.1$, and lepton coupling $g_l = 0.01$, in both cases universal to all flavours. Dashed curves labelled "thermal relic" correspond to combinations of DM and mediator mass values that are consistent with a DM density of $\Omega h^2 = 0.12$ and a standard thermal history as computed in MadDM [Phys. Dark Univ. **26** (2019) 100377, AIP Conf. Proc. **1743** (2016) 1, 060001]. Between the two dashed curves, annihilation processes described by the simplified model deplete Ωh^2 to below 0.12. The dotted line indicates the kinematic threshold where the mediator can decay on-shell into DM.

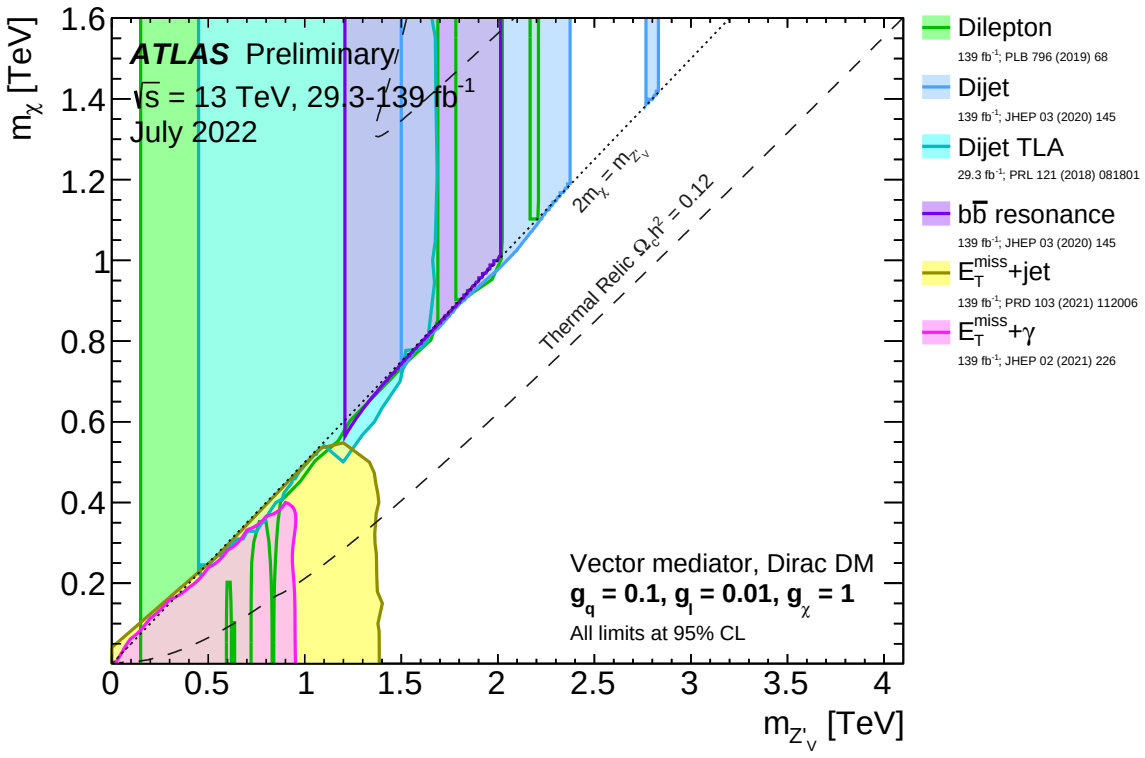

Figure 8: Regions in the (mediator-mass, DM-mass) plane excluded at 95% CL by dijet, dilepton and $E_{\mathrm{T}}^{\mathrm{miss}}+X$ searches, for leptophilic vector mediator simplified models. The exclusions are computed for a DM coupling $g_\chi = 1$, quark coupling $g_q = 0.1$, and lepton coupling $g_l = 0.01$, in both cases universal to all flavours. Dashed curves labelled "thermal relic" correspond to combinations of DM and mediator mass values that are consistent with a DM density of $\Omega h^2 = 0.12$ and a standard thermal history as computed in MadDM [Phys. Dark Univ. **26** (2019) 100377, AIP Conf. Proc. **1743** (2016) 1, 060001]. Between the two dashed curves, annihilation processes described by the simplified model deplete Ωh^2 to below 0.12. The dotted line indicates the kinematic threshold where the mediator can decay on-shell into DM.

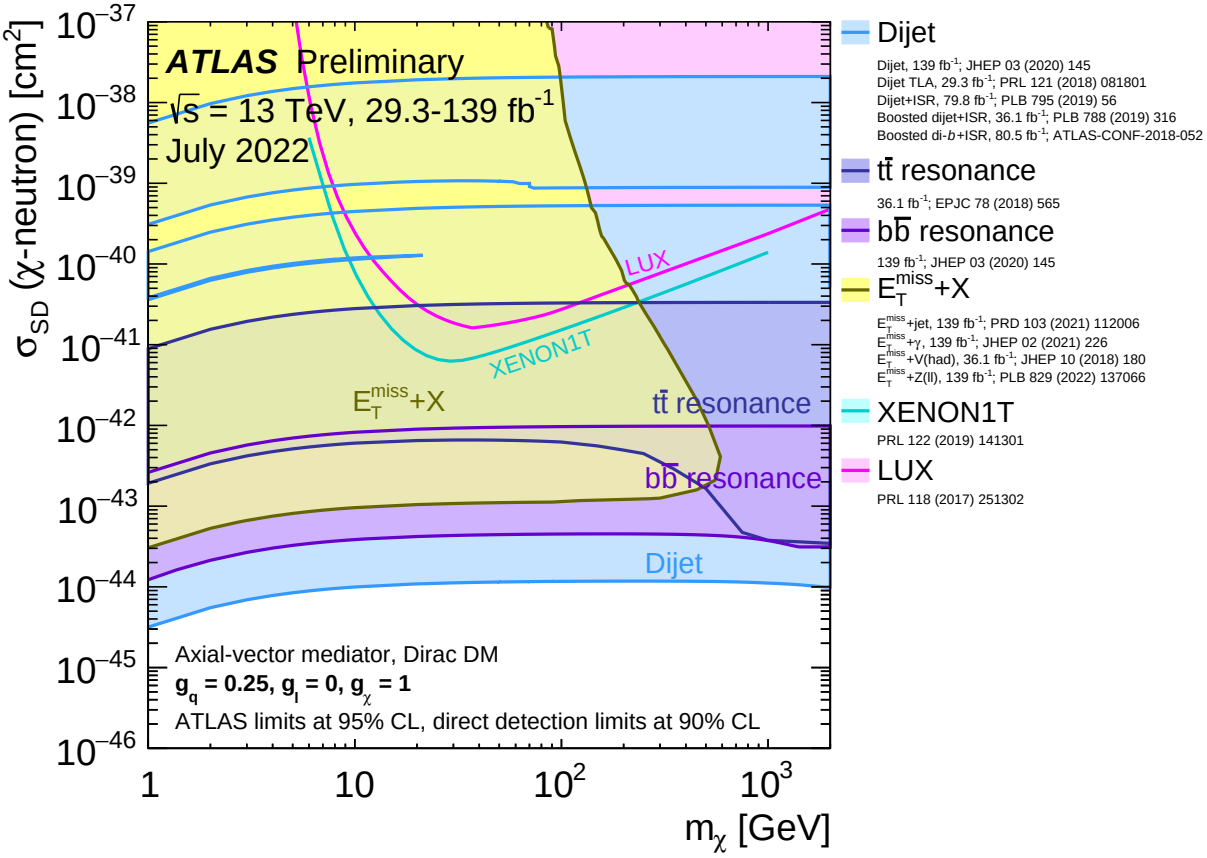

Figure 9: A comparison of the inferred limits with the constraints from direct-detection experiments on the spin-dependent WIMP–neutron cross-section in the context of the leptophobic axial-vector mediator simplified model. Each shaded region represents the union of the exclusion contours of the individual analyses listed in the legend, where more than one result contributes. The results from this analysis are compared with limits from direct-detection experiments. LHC limits are shown at 95% CL and direct-detection limits at 90% CL. The comparison is valid solely in the context of this model, assuming a mediator width fixed by the dark matter mass, a DM coupling $g_\chi = 1$, quark coupling $g_q = 0.25$, and no coupling to leptons. LHC searches and direct-detection experiments exclude the shaded areas. Exclusions of smaller scattering cross-sections do not imply that larger scattering cross-sections are also excluded. The resonance and $E_{\mathrm{T}}^{\mathrm{miss}}+X$ exclusion regions represent the union of exclusions from all analyses of that type.

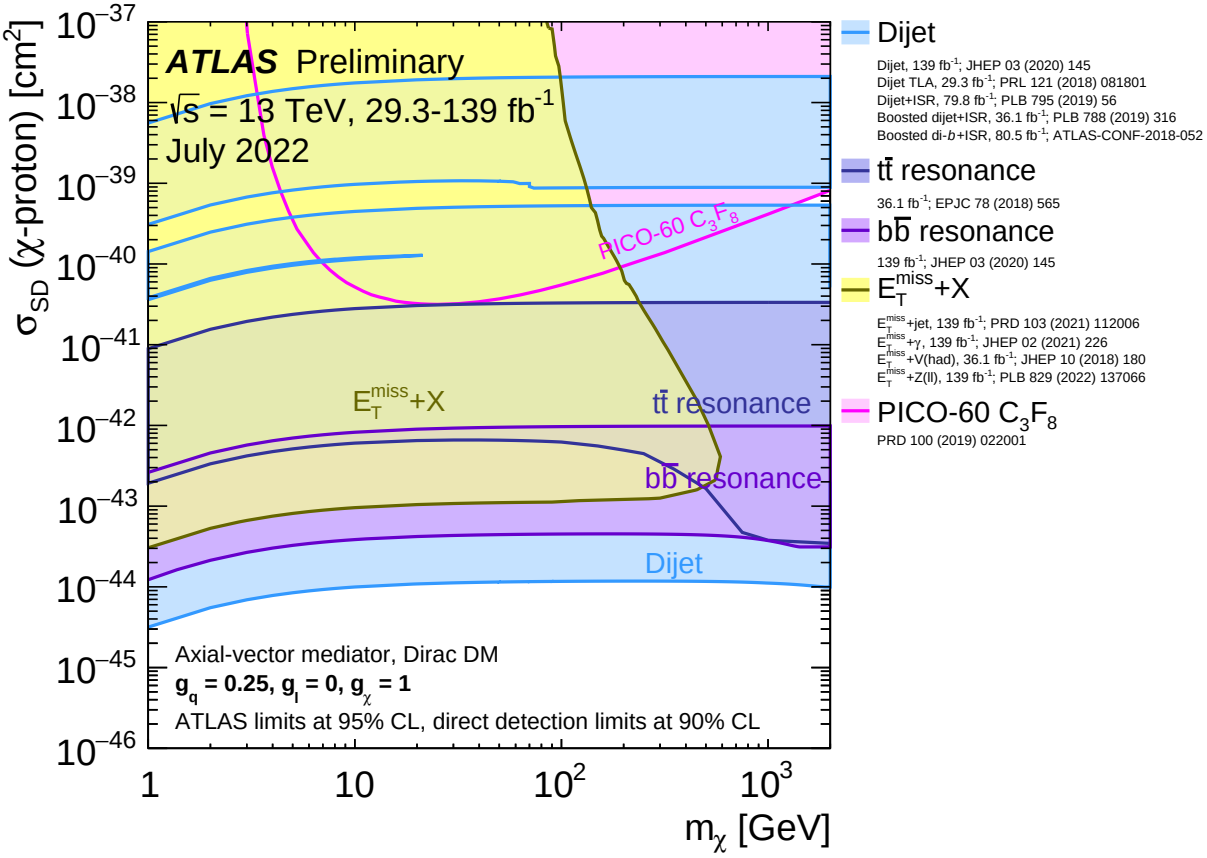

Figure 10: A comparison of the inferred limits with the constraints from direct-detection experiments on the spin-dependent WIMP–proton cross-section in the context of the leptophobic axial-vector mediator simplified model. Each shaded region represents the union of the exclusion contours of the individual analyses listed in the legend, where more than one result contributes. The results from this analysis are compared with limits from direct-detection experiments. LHC limits are shown at 95% CL and direct-detection limits at 90% CL. The comparison is valid solely in the context of this model, assuming a mediator width fixed by the dark matter mass, a DM coupling $g_\chi = 1$, quark coupling $g_q = 0.25$, and no coupling to leptons. LHC searches and direct-detection experiments exclude the shaded areas. Exclusions of smaller scattering cross-sections do not imply that larger scattering cross-sections are also excluded. The resonance and $E_{\mathrm{T}}^{\mathrm{miss}}+X$ exclusion regions represent the union of exclusions from all analyses of that type.

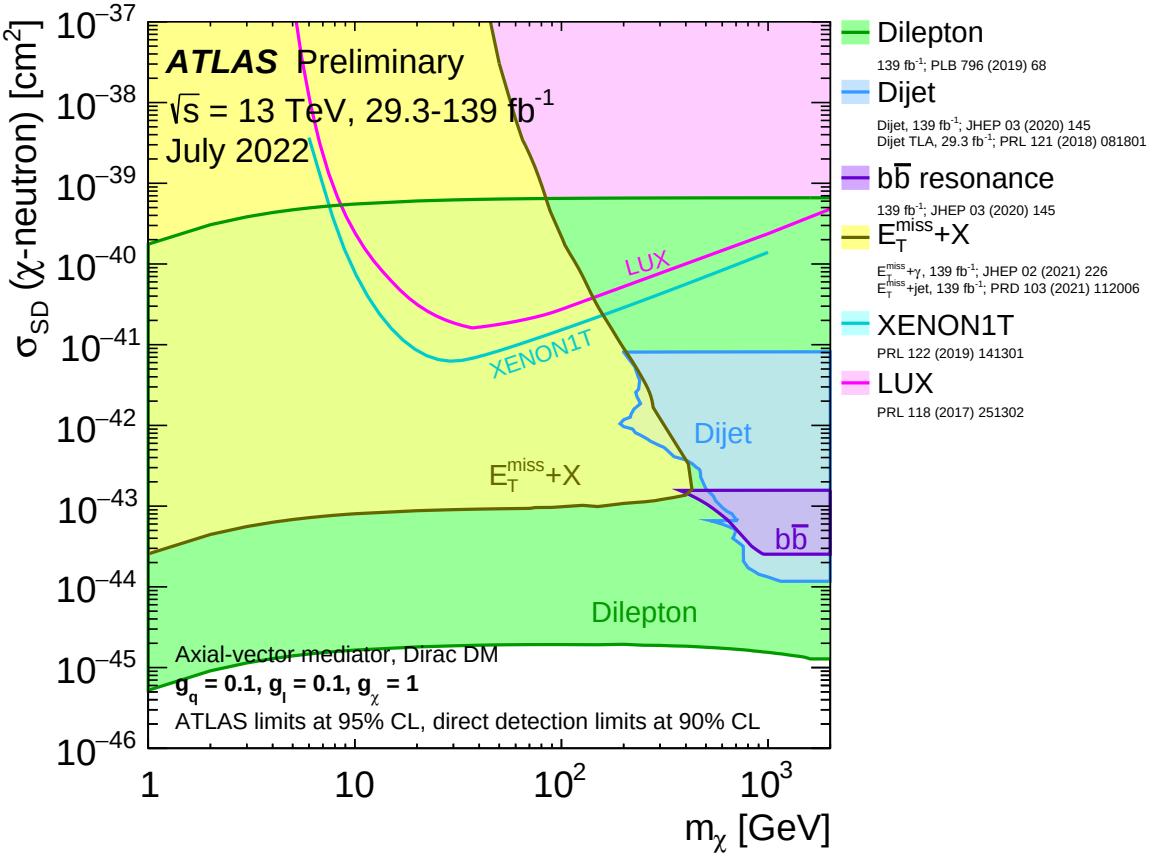

Figure 11: A comparison of the inferred limits with the constraints from direct-detection experiments on the spin-dependent WIMP–neutron scattering cross-section in the context of the leptophilic axial-vector mediator simplified model. Each shaded region represents the union of the exclusion contours of the individual analyses listed in the legend, where more than one result contributes. The results from this analysis are compared with limits from the direct-detection experiments. LHC limits are shown at 95% CL and direct-detection limits at 90% CL. The comparison is valid solely in the context of this model, assuming a mediator width fixed by the dark matter mass, a DM coupling $g_\chi = 1$, quark coupling $g_q = 0.1$, and lepton coupling $g_l = 0.1$. LHC searches and direct-detection experiments exclude the shaded areas. Exclusions of smaller scattering cross-sections do not imply that larger scattering cross-sections are also excluded. The resonance and $E_{\mathrm{T}}^{\mathrm{miss}}+X$ exclusion region represents the union of exclusions from all analyses of that type.

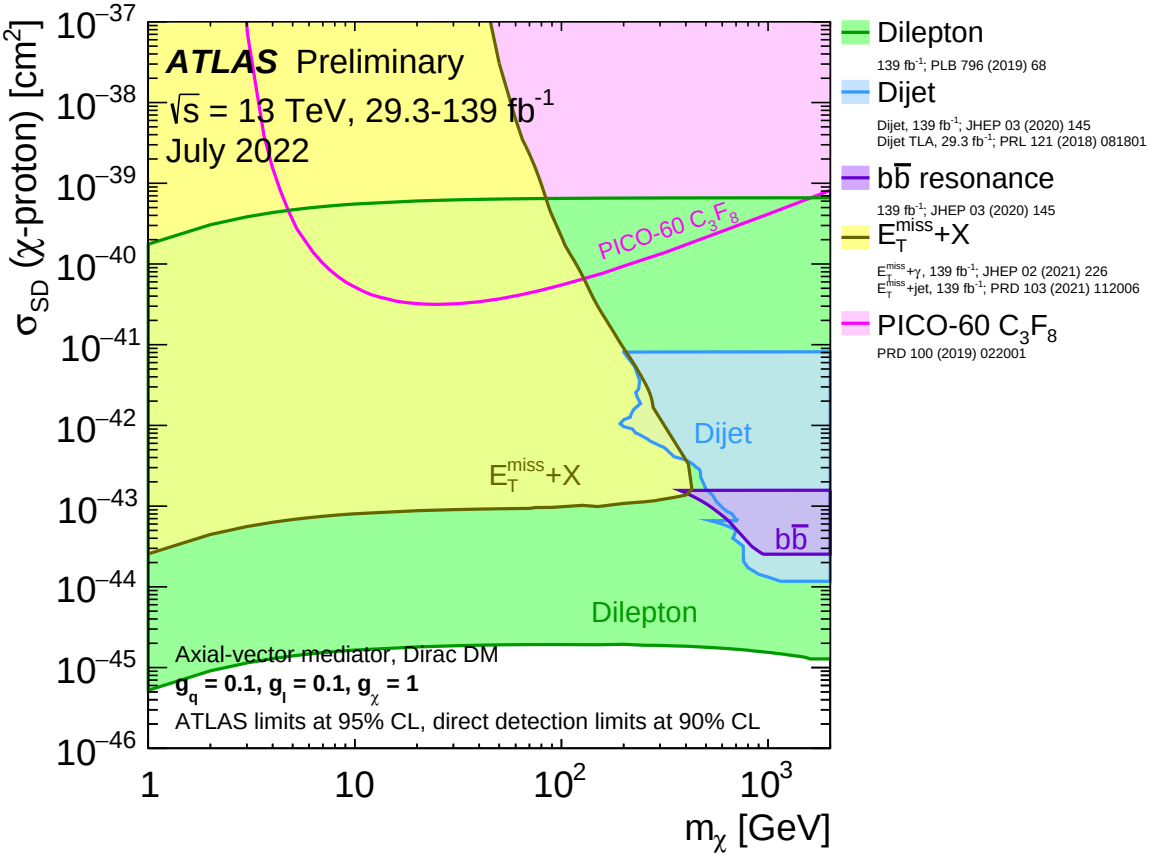

Figure 12: A comparison of the inferred limits with the constraints from direct-detection experiments on the spin-dependent WIMP–proton scattering cross-section in the context of the leptophilic axial-vector mediator simplified model. Each shaded region represents the union of the exclusion contours of the individual analyses listed in the legend, where more than one result contributes. The results from this analysis are compared with limits from the direct-detection experiments. LHC limits are shown at 95% CL and direct-detection limits at 90% CL. The comparison is valid solely in the context of this model, assuming a mediator width fixed by the dark matter mass, a DM coupling $g_\chi = 1$, quark coupling $g_q = 0.1$, and lepton coupling $g_l = 0.1$. LHC searches and direct-detection experiments exclude the shaded areas. Exclusions of smaller scattering cross-sections do not imply that larger scattering cross-sections are also excluded. The resonance and $E_{\mathrm{T}}^{\mathrm{miss}}+X$ exclusion region represents the union of exclusions from all analyses of that type.

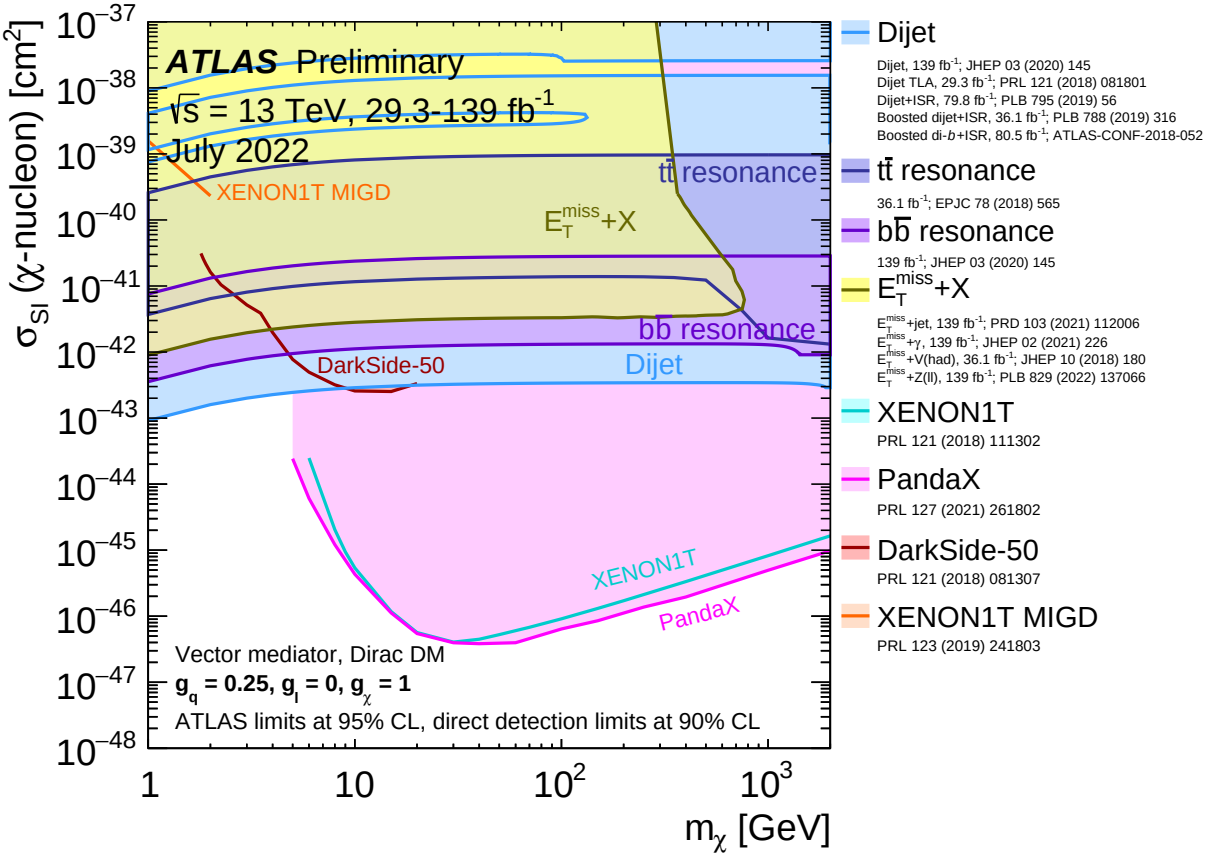

Figure 13: A comparison of the inferred limits with the constraints from direct-detection experiments on the spin-independent WIMP–nucleon scattering cross-section in the context of the leptophobic vector mediator simplified model. Each shaded region represents the union of the exclusion contours of the individual analyses listed in the legend, where more than one result contributes. The results from this analysis are compared with limits from the direct-detection experiments. LHC limits are shown at 95% CL and direct-detection limits at 90% CL. The comparison is valid solely in the context of this model, assuming a mediator width fixed by the dark matter mass, a DM coupling $g_\chi = 1$, quark coupling $g_q = 0.25$, and no coupling to leptons. LHC searches and direct-detection experiments exclude the shaded areas. Exclusions of smaller scattering cross-sections do not imply that larger scattering cross-sections are also excluded. The resonance and $E_{\mathrm{T}}^{\mathrm{miss}}+X$ exclusion region represents the union of exclusions from all analyses of that type.

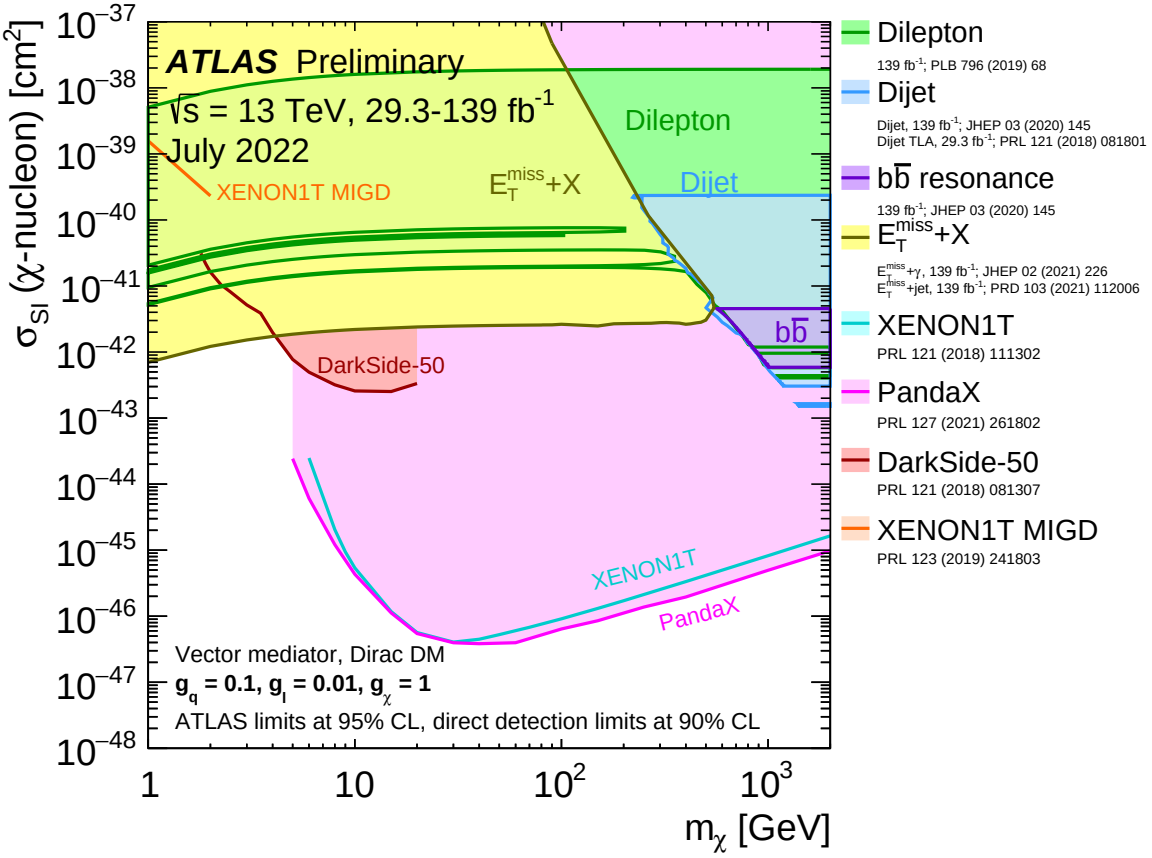

Figure 14: A comparison of the inferred limits with the constraints from direct-detection experiments on the spin-independent WIMP–nucleon scattering cross-section in the context of the leptophilic vector mediator simplified model. Each shaded region represents the union of the exclusion contours of the individual analyses listed in the legend, where more than one result contributes. The results from this analysis are compared with limits from the direct-detection experiments. LHC limits are shown at 95% CL and direct-detection limits at 90% CL. The comparison is valid solely in the context of this model, assuming a mediator width fixed by the dark matter mass, a DM coupling $g_\chi = 1$, quark coupling $g_q = 0.1$, and lepton coupling $g_l = 0.01$. LHC searches and direct-detection experiments exclude the shaded areas. Exclusions of smaller scattering cross-sections do not imply that larger scattering cross-sections are also excluded. The resonance and $E_{\mathrm{T}}^{\mathrm{miss}}+X$ exclusion region represents the union of exclusions from all analyses of that type.

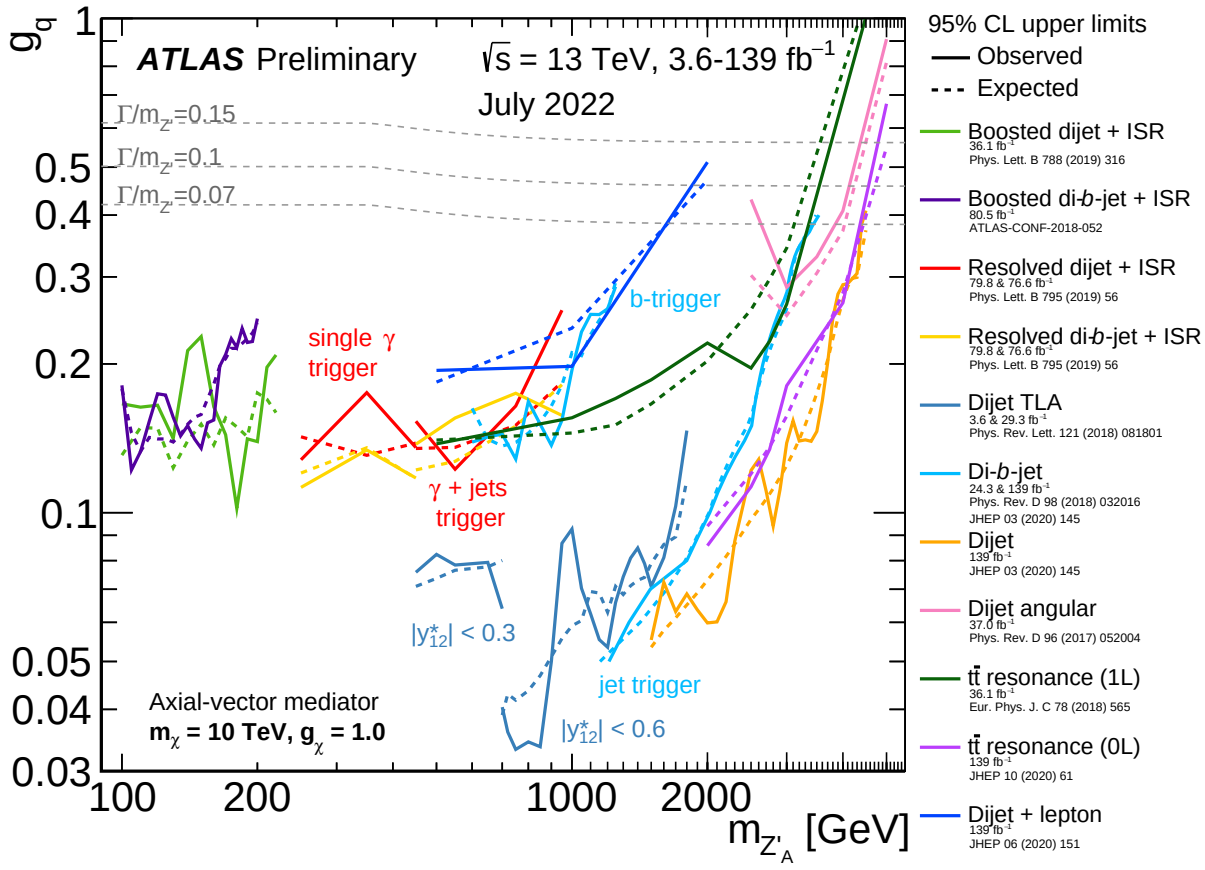

Figure 15: Hadronic resonance search contours for 95% CL upper limits on the coupling g_q as a function of the resonance mass $m_{Z'_A}$ for the leptophilic axial-vector mediator simplified model. The expected limits from each search are indicated by dotted lines. The TLA dijet analysis has two parts, employing different datasets with different selections in the rapidity difference y^* as indicated. The dijet+ISR (γ) analysis also has two parts, each using a different trigger strategy, and each further studied in inclusive and b-tagged channels. Two lines are also shown for the di-b-jet search. These are from separate analyses, one which used b-jet triggers and provides the limit at lower mass, and one which used inclusive jet triggers and provides the high mass limit. Coupling values above the solid lines are excluded, as long as the signals are narrow enough to be detected using these searches. The TLA dijet search with $|y^*| < 0.6$ is sensitive up to $\Gamma/m_{Z'} = 7\%$, the TLA dijet with $|y^*| < 0.3$ and dijet + ISR searches are sensitive up to $\Gamma/m_{Z'} = 10\%$, and the dijet and di-b-jet searches are sensitive up to $\Gamma/m_{Z'} = 15\%$. The dijet angular analysis is sensitive up to $\Gamma/m_{Z'} = 50\%$. No limitation in sensitivity arises from large width resonances in the $t\bar{t}$ resonance analysis. Benchmark width lines are indicated in the canvas. $\Gamma/m_{Z'} = 50\%$ lies beyond the canvas borders.

2.2 Spin-0 Mediators

This section provides dark matter summary plots from analyses targetting exotic and supersymmetric signal models. This section refers to a signal model which includes a Dirac fermion dark matter candidate, χ, and a new spin-zero particle, $\phi(a)$, which couples to Dark Matter and quarks with a new spin-zero scalar (pseudoscalar) particle [1, 6, 7]. Assuming minimal flavour violation [8], the model assumes a Yukawa-like structure of the couplings of the new mediator to the SM particles, which include a common coupling g_q. The additional free parameters of the model are the masses of the Dark Matter m_χ, the mediator particles m_ϕ/m_a, and the coupling strength of the interactions between the mediator particle and Dark Matter particles g_χ.

A more detailed description of the models considered in Figures 16 and 17 is now presented:

***Model 1*:** considers scalar and pseudoscalar mediators produced in association with a pair of bottom quarks (DMbb). The production cross-sections for these models were evaluated including NLO QCD corrections assuming SM Yukawa couplings to quarks, in a five-flavour scheme, following Ref. [9].

***Model 2*:** Scalar and pseudoscalar signal samples were simulated in POWHEG BOX [10–12] using a simplified model implementation described in Ref. [13]. The DMS_tloop model was used for the production with s-channel spin-0 scalar and pseudoscalar mediator exchange with the full quark-loop calculation at LO [14].

***Model 3*:** considers scalar and pseudoscalar mediators produced in association with a pair of top quarks (DMtt) and, in addition, single top quark production referred as DMt. Both productions use *DMsimp* implementation [15]. Signal samples for DMtt are generated using a LO matrix element, with up to one extra parton using the MADGRAPH5_AMC@NLO [16] generator interfaced to PYTHIA and using the CKKW-L merging algorithm [17]. The top quark decay is simulated using MADSPIN [18]. Signal cross sections for the DMtt process are calculated to NLO QCD accuracy using the same version of MADGRAPH, as suggested in Ref. [15]. Signal samples for dark matter associated production with a single top quark are generated using the same settings as the DMtt. No extra partons from the matrix element are generated in this case. DMt signal models are generated separately for tW and the tj processes. Each one is normalised to the LO cross section predicted by the model and then the samples are combined (added together).

With respect to the summary results for spin-0 mediators released for Moriond 2022 [4], new analyses have been released publicly and are described in detail below:

$b\bar{b}$+$E_{\mathrm{T}}^{\mathrm{miss}}$*0L:** The full Run 2 results is included in the current document [19]. No modification has been made for this analysis result. This analysis uses ***Model 1.

Monojet: The full Run 2 result for the jets+$E_{\mathrm{T}}^{\mathrm{miss}}$ analysis [20] were previously included but only presented for the pseudoscalar interpretation. This analysis uses ***Model 2***.

***$t\bar{t}$+$E_{\mathrm{T}}^{\mathrm{miss}}$*Combination:** Previously, results were presented for different leptonic final states explicitly [21–23]. A new result [24] is now included, consisting of a statistical combination of three searches targeting events with two top quarks and invisible particles considering either zero- (tt0L [25]), one- (tt1L [22]) or two-lepton (tt2L [23]) final states. The tt0L analysis is extended and improved with respect to Ref. [25] benefitting from the Run-2 improvements in the trigger selection of jets containing b-hadrons (b-jets) in ATLAS [26] that increases the sensitivity in models with light mediator masses. These three analyses select independent (orthogonal) datasets and their statistical

combination boosts the sensitivity as they constrain similar parts of the parameter space. This analysis uses ***Model 3***.

tj*+$E_{\mathrm{T}}^{\mathrm{miss}}$1L, *tW*+$E_{\mathrm{T}}^{\mathrm{miss}}$1L, *tW*+$E_{\mathrm{T}}^{\mathrm{miss}}$2L** These three analysis selections were developed in the context of the 2HDM+*a* model as a search for single top quarks produced in association with DM candidates [27]. These analysis selections use ***Model 3.

The updated summaries are presented in Figures 16, and 17.

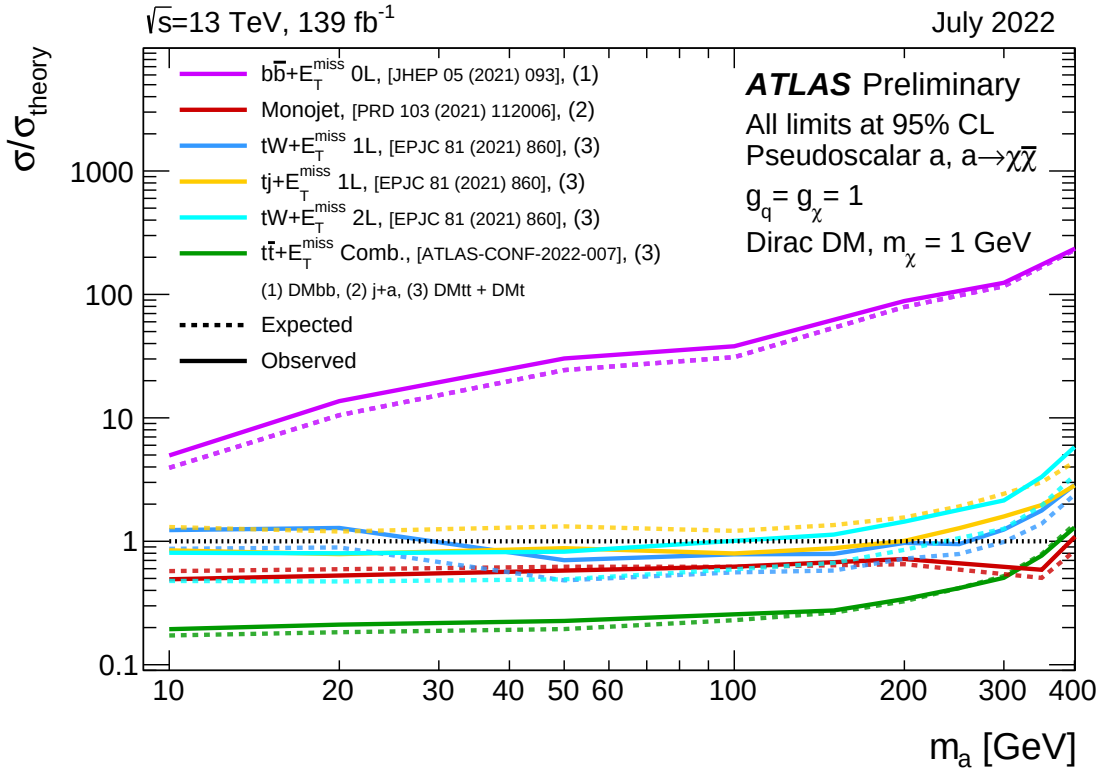

Figure 16: Exclusion limits for colour-neutral pseudoscalar mediator dark matter models [Phys. Dark Univ. **26** (2019) 100371] as a function of the mediator mass m_a for a dark matter mass m_χ of 1 GeV. The limits are calculated at 95% CL and are expressed in terms of the ratio of the excluded cross-section to the nominal cross-section for a coupling assumption of $g_q = g_\chi = 1$. The solid (dashed) lines show the observed (expected) exclusion limits for different analyses. The $b\bar{b}$+$E_{\mathrm{T}}^{\mathrm{miss}}$0L analysis considers the DMbb signal model. The $t\bar{t}$+$E_{\mathrm{T}}^{\mathrm{miss}}$ combination, tj+$E_{\mathrm{T}}^{\mathrm{miss}}$1L, tW+$E_{\mathrm{T}}^{\mathrm{miss}}$1L and tW+$E_{\mathrm{T}}^{\mathrm{miss}}$2L analyses consider DMtt and DMt signal models. Signal cross-sections for the DMtt process are calculated to NLO QCD accuracy while the DMt process is calculated to LO accuracy. The monojet analysis considers the $j + a$ signal model.

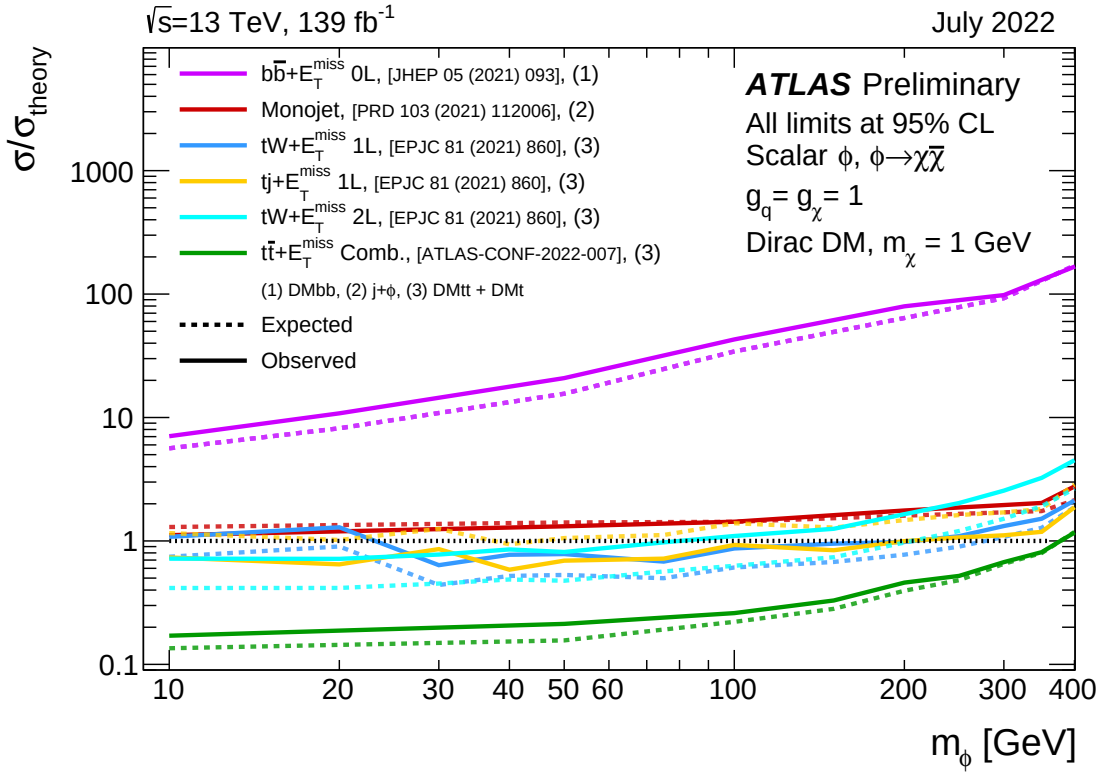

Figure 17: Exclusion limits for colour-neutral scalar mediator dark matter models [Phys. Dark Univ. **26** (2019) 100371] as a function of the mediator mass m_ϕ for a dark matter mass m_χ of 1 GeV. The limits are calculated at 95% CL and are expressed in terms of the ratio of the excluded cross-section to the nominal cross-section for a coupling assumption of $g_q = g_\chi = 1$. The solid (dashed) lines show the observed (expected) exclusion limits for different analyses. The $b\bar{b}$+$E_{\mathrm{T}}^{\mathrm{miss}}$0L analysis consider the DMbb signal model. The $t\bar{t}$+$E_{\mathrm{T}}^{\mathrm{miss}}$ combination, tj+$E_{\mathrm{T}}^{\mathrm{miss}}$1L, tW+$E_{\mathrm{T}}^{\mathrm{miss}}$1L and tW+$E_{\mathrm{T}}^{\mathrm{miss}}$2L analyses consider DMtt and DMt signal models. Signal cross-sections for the DMtt process are calculated to NLO QCD accuracy while the DMt process is calculated to LO accuracy. The monojet analysis considers the $j + \phi$ signal model.

3 2HDM+a summary plots

This section provide the 2HDM+a [2] summary plots. With respect to the results released for the Moriond 2022 conference [4], only one reference to a public result has been updated:

$\boldsymbol{E_{\mathrm{T}}^{\mathrm{miss}} + Z(\ell^+\ell^-)}$: Shown with the paper publication reference (Ref. [5] replacing [arXiv:2111.08372]).

3.1 Overview of parameter scans

The following parameter scans released in Ref. [28] are included:

- **Scan 1**: two 2D scans in (m_a, m_A) assuming $\tan\beta = 1.0$ and
  a. $\sin\theta = 0.35$
  b. $\sin\theta = 0.7$.
- **Scan 2**: two 2D scans in $(m_A, \tan\beta)$ assuming $m_a = 250$ GeV and
  a. $\sin\theta = 0.35$
  b. $\sin\theta = 0.7$.
- **Scan 3**: two 2D scans in $(m_a, \tan\beta)$ assuming $m_A = 0.6$ TeV and
  a. $\sin\theta = 0.35$
  b. $\sin\theta = 0.7$.
- **Scan 4**: two 1D scans in $\sin\theta$ with $\tan\beta = 1.0$ and
  a. $m_A = 0.6$ TeV, $m_a = 200$ GeV (low-mass scan)
  b. $m_A = 1$ TeV, $m_a = 350$ GeV (high-mass scan)
- **Scan 5**: a 1D scan in m_χ assuming $m_A = 0.6$ TeV, $m_a = 250$ GeV, $\tan\beta = 1.0$ and $\sin\theta = 0.35$.

In all scans other than the DM mass scan, $m_\chi = 10$ GeV is chosen. The choice of m_χ has a negligible impact on the $E_{\mathrm{T}}^{\mathrm{miss}}$+X signatures for $m_a > 2m_\chi$. The chosen value ensures a sizeable branching ratio for the decay $a \to \chi\bar{\chi}$ for all values of $m_a > 100$ GeV that are considered in this note.

3.2 Results

m_A-m_a scan

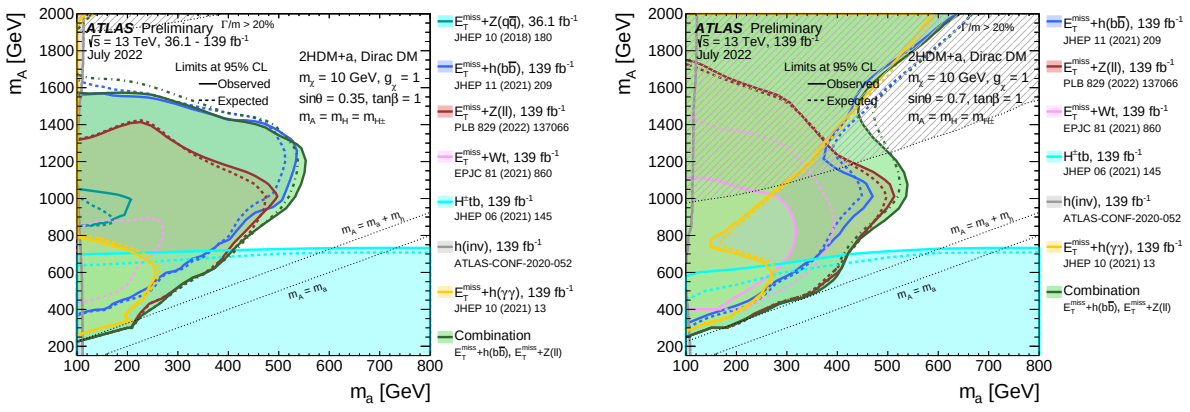

(a) (b)

Figure 18: Observed (solid lines) and expected (dashed lines) exclusion regions at 95% CL in the (m_a, m_A) plane under the assumption of (a) $\sin\theta = 0.35$ (scan 1a) and (b) $\sin\theta = 0.7$ (scan 1b). The results are shown for several individual searches as well as the combination of the $E_{\mathrm{T}}^{\mathrm{miss}} + Z(\ell^+\ell^-)$ and $E_{\mathrm{T}}^{\mathrm{miss}} + h(b\bar{b})$ searches. The dashed grey regions indicate the region where the width of any of the Higgs bosons exceeds 20% of its mass. The larger exclusions of $E_{\mathrm{T}}^{\mathrm{miss}} + h(b\bar{b})$ and $E_{\mathrm{T}}^{\mathrm{miss}} + h(\gamma\gamma)$ in high m_A region are due to an increase of the cross section of the $a \to ah$ process, which are more significant when $\sin\theta = 0.7$. The observed exclusion of $E_{\mathrm{T}}^{\mathrm{miss}}$+$Wt$ search is weaker than the expected sensitivity due to a small (within 2σ) excess in the $tW_{2\mathrm{L}}$ region [27]. Thus in Figure 18(a), no observed exclusion is shown in the parameter space.

$\tan\beta$ -m_A scan

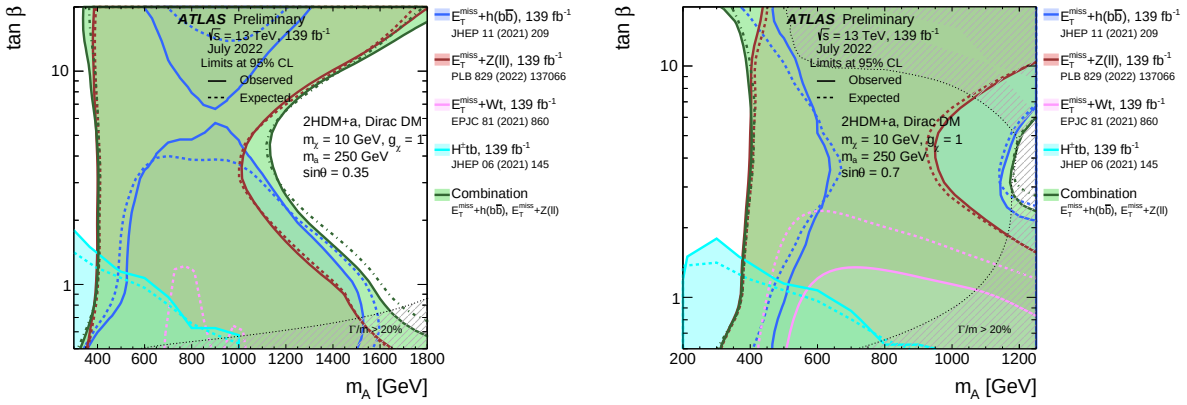

(a) (b)

Figure 19: Observed (solid lines) and expected (dashed lines) exclusion regions at 95% CL in the $(m_A, \tan\beta)$ plane under the assumption of (a) $\sin\theta = 0.35$ (scan 2a) and (b) $\sin\theta = 0.7$ (scan 2b). The results are shown for several individual searches as well as the combination of the $E_{\mathrm{T}}^{\mathrm{miss}} + Z(\ell^+\ell^-)$ and $E_{\mathrm{T}}^{\mathrm{miss}} + h(b\bar{b})$ searches. The dashed grey regions indicate the region where the width of any of the Higgs bosons exceeds 20% of its mass. The observed exclusion of $E_{\mathrm{T}}^{\mathrm{miss}}$+$Wt$ search is weaker than the expected sensitivity due to a small (within 2σ) excess in the $tW_{2\mathrm{L}}$ region [27]. Thus in Figure 19(a), no observed exclusion is shown in the parameter space.

$\tan\beta$ -m_a scan

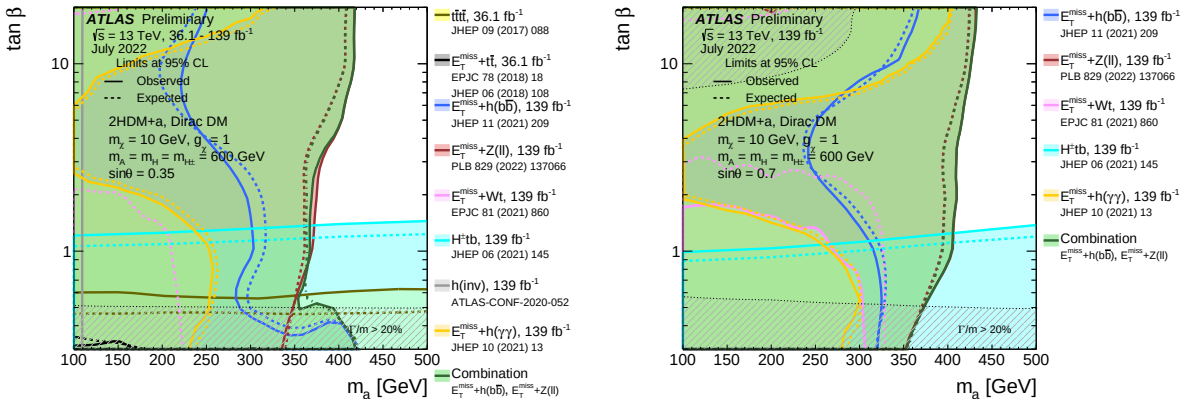

(a) (b)

Figure 20: Observed (solid lines) and expected (dashed lines) exclusion regions at 95% CL in the $(m_a, \tan\beta)$ plane under the assumption of (a) $\sin\theta = 0.35$ (scan 3a) and (b) $\sin\theta = 0.7$ (scan 3b). The results are shown for several individual searches as well as the combination of the $E_{\mathrm{T}}^{\mathrm{miss}} + Z(\ell^+\ell^-)$ and $E_{\mathrm{T}}^{\mathrm{miss}} + h(b\bar{b})$ searches. The dashed grey regions indicate the region where the width of any of the Higgs bosons exceeds 20% of its mass. The observed exclusion of $E_{\mathrm{T}}^{\mathrm{miss}}$+$Wt$ search is weaker than the expected sensitivity due to a small (within 2σ) excess in the $tW_{2\mathrm{L}}$ region [27]. Thus in Figure 20(a), no observed exclusion is shown in the parameter space.

sin θ scan

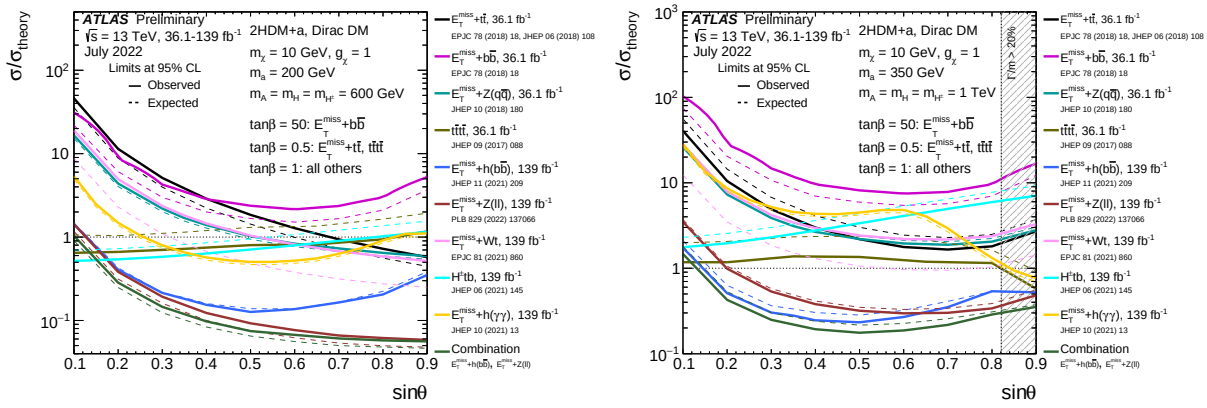

(a) (b)

Figure 21: Observed (solid lines) and expected (dashed lines) exclusion limits at 95% CL for the 2HDM+a model as a function of $\sin\theta$, for $\tan\beta = 1.0$ and (a) $m_A = 0.6$ TeV , $m_a = 200$ GeV (scan 4a: low-mass hypothesis) and (b) $m_A = 1.0$ TeV , $m_a = 350$ GeV (scan 4b: high-mass hypothesis). The results are shown for several individual searches as well as the combination of the $E_{\mathrm{T}}^{\mathrm{miss}} + Z(\ell^+\ell^-)$ and $E_{\mathrm{T}}^{\mathrm{miss}} + h(b\bar{b})$ searches.

m_χ scan

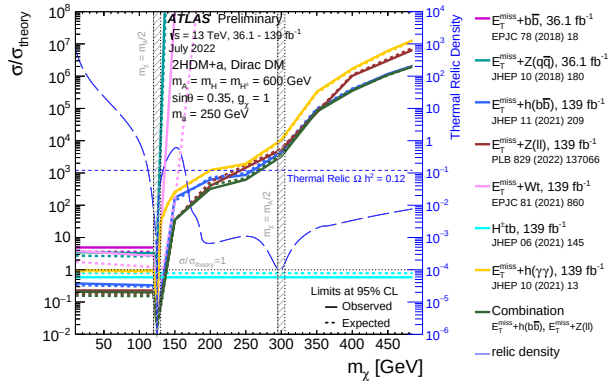

Figure 22: Observed (solid lines) and expected (dashed lines) exclusion limits for the 2HDM+a model as a function of m_χ , following the parameter choices of $m_A = 0.6$ TeV, $m_a = 250$ GeV, $\tan\beta = 1.0$ and $\sin\theta = 0.35$ (scan 5). The limits are calculated at 95% CL and are expressed in terms of the ratio of the excluded cross section to the nominal cross section of the model. The results are shown for several individual searches as well as the combination of the $E_{\mathrm{T}}^{\mathrm{miss}} + Z(\ell^+\ell^-)$ and $E_{\mathrm{T}}^{\mathrm{miss}} + h(b\bar{b})$ searches. The relic density for each m_χ assumption is superimposed in the plot (long-dashed line) and described by the right vertical axis. For dark matter mass values where the relic density line is below $\Omega h^2 = 0.12$, the model depletes the relic density to below the thermal value. The two valleys at $m_\chi = 125$ GeV and $m_\chi = 300$ GeV determine the two a-funnel and A-funnel regions [2, 29, 30] where the predicted relic density is depleted by the resonant enhancement of the processes $\chi\bar{\chi} \to A/a \to$ SM. The shaded region around 125 GeV indicates a ±5 GeV band around the kinematic thresholds $m_\chi = m_a/2$ and $m_\chi = m_A/2$ where the generator results are deemed unreliable. The interpolation of the exclusion limit for the $E_{\mathrm{T}}^{\mathrm{miss}} + h$ and $E_{\mathrm{T}}^{\mathrm{miss}} + Z$ searches in the region 125-150 GeV in m_χ is subject to large uncertainties due to the rapidly changing cross sections in this region.

4 Dark Higgs summary plot

This section provides a new summary plot from analyses targetting the Dark Higgs Model [3]. This signal model provides a Majorana fermion dark matter candidate χ and two mediators: a vector boson Z' and a scalar dark Higgs boson s. The dark Higgs boson does not couple to SM particles, but can decay via mixing with the SM Higgs boson and hence has SM-like branching fractions as long as there are no new decay channels. The additional free parameters of this model are the masses of the Dark Matter m_χ, the mediator particles $m_{Z'}$ and m_s, the Z' coupling strength to quarks q_q and to DM g_χ, and the mixing angle θ between the SM and dark Higgs bosons.

4.1 Parameter scan

The following parameter scan has been added:

- **Scan1**: a scan in $(m_{Z'}, m_s)$ assuming $g_q = 0.25$, $g_\chi = 1$, $\sin\theta = 0.01$, $m_\chi = 200$ GeV. This scan is shown in Figure 23.

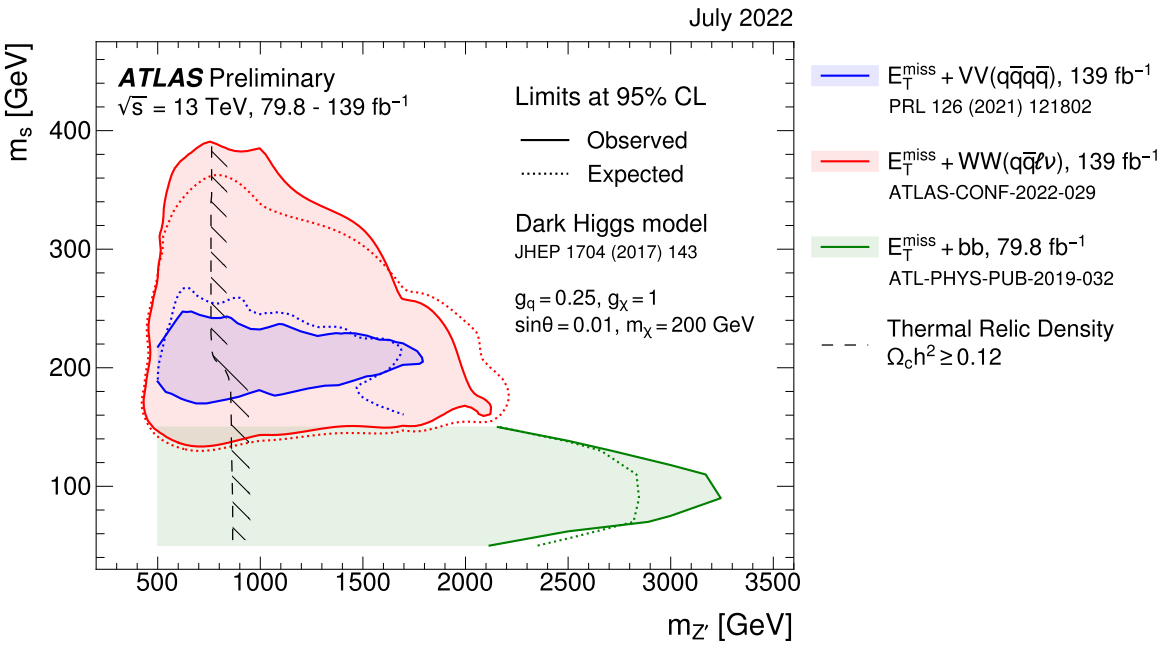

Figure 23: Observed (solid lines) and expected (dotted lines) exclusion limits at 95% CL for the Dark Higgs model in the $(m_{Z'}, m_s)$ plane under the assumption of $g_q = 0.25$, $g_\chi = 1$, $\sin\theta = 0.01$, $m_\chi = 200$ GeV. The open contours indicates regions of the mass plane not explored for that particular signature. The coloured areas are excluded. The dashed curve corresponds to the combinations of parameter values that are consistent with a DM density of $\Omega h^2 = 0.12$ and a standard thermal history, as computed in MadDM [Phys. Dark Univ. **26** (2019) 100377, AIP Conf. Proc. **1743** (2016) 1, 060001], with the diagonal lines indicating which side corresponds to an overabundance of DM.

References

[1] D. Abercrombie et al., *Dark Matter benchmark models for early LHC Run-2 Searches: Report of the ATLAS/CMS Dark Matter Forum*, Phys. Dark Univ. **26** (2019) 100371, arXiv: 1507.00966 [hep-ex].

[2] T. Abe et al., *LHC Dark Matter Working Group: Next-generation spin-0 dark matter models*, Phys. Dark Univ. **27** (2020) 100351, arXiv: 1810.09420 [hep-ex].

[3] M. Duerr et al., *Hunting the dark Higgs*, JHEP **04** (2017) 143, arXiv: 1701.08780 [hep-ph].

[4] ATLAS Collaboration, *Dark matter summary plots for s-channel and 2hdm+a models*, ATL-PHYS-PUB-2021-045, 2021, URL: https://cds.cern.ch/record/2798737.

[5] ATLAS Collaboration, *Search for associated production of a Z boson with an invisibly decaying Higgs boson or dark matter candidates at $\sqrt{s}$ = 13 TeV with the ATLAS detector*, Phys. Lett. B **829** (2022) 137066, arXiv: 2111.08372 [hep-ex].

[6] M. R. Buckley, D. Feld and D. Goncalves, *Scalar simplified models for dark matter*, Phys. Rev. D **91** (2015), arXiv: 1410.6497 [hep-ph].

[7] U. Haisch and E. Re, *Simplified dark matter top-quark interactions at the LHC*, JHEP **06** (2015) 078, arXiv: 1503.00691 [hep-ph].

[8] ATLAS Collaboration, *Constraints on mediator-based dark matter and scalar dark energy models using $\sqrt{s}$ = 13 TeV pp collision data collected by the ATLAS detector*, JHEP **05** (2019) 142, arXiv: 1903.01400 [hep-ex].

[9] Y. Afik et al., *DM+$b\bar{b}$ simulations with DMSimp: an update*, 2018, arXiv: 1811.08002 [hep-ex].

[10] S. Alioli, P. Nason, C. Oleari and E. Re, *A general framework for implementing NLO calculations in shower Monte Carlo programs: the POWHEG BOX*, JHEP **06** (2010) 043, arXiv: 1002.2581 [hep-ph].

[11] S. Frixione, P. Nason and C. Oleari, *Matching NLO QCD computations with parton shower simulations: the POWHEG method*, JHEP **11** (2007) 070, arXiv: 0709.2092 [hep-ph].

[12] P. Nason, *A new method for combining NLO QCD with shower Monte Carlo algorithms*, JHEP **11** (2004) 040, arXiv: hep-ph/0409146.

[13] U. Haisch, F. Kahlhöfer and E. Re, *QCD effects in mono-jet searches for dark matter*, JHEP **12** (2013) 007, arXiv: 1310.4491 [hep-ph].

[14] U. Haisch and E. Re, *Simplified dark matter top-quark interactions at the LHC*, JHEP **06** (2015) 078, arXiv: 1503.00691 [hep-ph].

[15] M. Backovic et al., *Higher-order QCD predictions for dark matter production at the LHC in simplified models with s-channel mediators*, Eur. Phys. J. C **75** (2015) 482, arXiv: 1508.05327 [hep-ph].

[16] J. Alwall et al., *The automated computation of tree-level and next-to-leading order differential cross sections, and their matching to parton shower simulations*, JHEP **07** (2014) 079, arXiv: 1405.0301 [hep-ph].

[17] L. Lönnblad, *Correcting the Colour-Dipole Cascade Model with Fixed Order Matrix Elements*, JHEP **05** (2002) 046, arXiv: hep-ph/0112284.

[18] P. Artoisenet, R. Frederix, O. Mattelaer and R. Rietkerk, *Automatic spin-entangled decays of heavy resonances in Monte Carlo simulations*, JHEP **03** (2013) 015, arXiv: 1212.3460 [hep-ph].

[19] ATLAS Collaboration, *Search for new phenomena in final states with b-jets and missing transverse momentum in $\sqrt{s}$ = 13 TeV pp collisions with the ATLAS detector*, JHEP **05** (2021) 093, arXiv: 2101.12527 [hep-ex].

[20] ATLAS Collaboration, *Search for new phenomena in events with an energetic jet and missing transverse momentum in pp collisions at $\sqrt{s}$ = 13 TeV with the ATLAS detector*, Phys. Rev. D **103** (2021) 112006, arXiv: 2102.10874 [hep-ex].

[21] ATLAS Collaboration, *Search for dark matter produced in association with bottom or top quarks in $\sqrt{s}$ = 13 TeV pp collisions with the ATLAS detector*, Eur. Phys. J. C **78** (2018) 18, arXiv: 1710.11412 [hep-ex].

[22] ATLAS Collaboration, *Search for new phenomena with top quark pairs in final states with one lepton, jets, and missing transverse momentum in pp collisions at $\sqrt{s}$ = 13 TeV with the ATLAS detector*, JHEP **04** (2020) 174, arXiv: 2012.03799 [hep-ex].

[23] ATLAS Collaboration, *Search for new phenomena in events with two opposite-charge leptons, jets and missing transverse momentum in pp collisions at $\sqrt{s}$ = 13 TeV with the ATLAS detector*, JHEP **04** (2021) 165, arXiv: 2102.01444 [hep-ex].

[24] ATLAS Collaboration, *Constraints on spin-0 dark matter mediators and invisible Higgs decays using ATLAS 13 TeV pp collision data with two top quarks and missing energy in the final state*, ATLAS-CONF-2022-007, 2022, URL: https://cds.cern.ch/record/2805211.

[25] ATLAS Collaboration, *Search for a scalar partner of the top quark in the all-hadronic $t\bar{t}$ plus missing transverse momentum final state at $\sqrt{s}$ = 13 TeV with the ATLAS detector*, Eur. Phys. J. C **80** (2020) 737, arXiv: 2004.14060 [hep-ex].

[26] ATLAS Collaboration, *Configuration and performance of the ATLAS b-jet triggers in Run 2*, Eur. Phys. J. C **81** (2021) 1087, arXiv: 2106.03584 [hep-ex].

[27] ATLAS Collaboration, *Search for dark matter produced in association with a single top quark in $\sqrt{s}$ = 13 TeV pp collisions with the ATLAS detector*, Eur. Phys. J. C **81** (2020) 860, arXiv: 2011.09308 [hep-ex].

[28] ATLAS Collaboration, *Combination and summary of ATLAS dark matter searches using 139 fb^{-1} of $\sqrt{s}$ = 13 TeV pp collision data and interpreted in a two-Higgs-doublet model with a pseudoscalar mediator*, ATLAS-CONF-2021-036, 2021, URL: https://cds.cern.ch/record/2777863.

[29] A. Djouadi, M. Drees and J.-L. Kneur, *Neutralino dark matter in mSUGRA: Reopening the light Higgs pole window*, Phys. Lett. B **624** (2005) 60, arXiv: hep-ph/0504090 [hep-ph].

[30] E. A. Bagnaschi et al., *Supersymmetric dark matter after LHC Run 1*, Eur. Phys. J. C **75** (2015) 500, arXiv: 1508.01173 [hep-ph].